

A Pixel Space Method for Testing Dipole Modulation in the CMB Polarization

Shamik Ghosh,^{1*} Pankaj Jain,^{1†}

¹*Dept. of Physics, Indian Institute of Technology, Kanpur - 208016, India*

Accepted XXX. Received YYY; in original form ZZZ

ABSTRACT

We introduce a pixel space method to detect dipole modulation or hemispherical power asymmetry in the cosmic microwave background (CMB) polarization. The method relies on the use of squared total polarized flux whose ensemble average picks up a dipole due to the dipole modulation in the CMB polarization. The method is useful since it can be applied easily to partial sky. We define several statistics to characterize the amplitude of the detected signal. By simulations we show that the method can be used to reliably extract the signal at $3\text{-}\sigma$ level in future CORe-like missions, assuming that the signal is present in the CMB polarization at the level detected by the Planck mission in the CMB temperature. An application of the method to the Planck data does not detect a significant effect. This may be due to the presence of a correlated detector noise or residual systematics in data. Using the half-ring half-difference (HRHD) maps and half-mission half-difference (HMHD) maps as our models for the detector noise we find the presence of a very strong bias which might be masking a real effect.

Key words: cosmic background radiation – cosmology: observation

1 INTRODUCTION

The hemispherical power asymmetry (HPA) is one of the most well known and well-studied anomaly observed in the cosmic microwave background (CMB) temperature fluctuation field. It is an important observation questioning the validity of the Cosmological Principle. The Cosmological Principle is an assumption that the spatial distribution of matter and radiation in the universe is statistically isotropic. The HPA is the observation that the power of the CMB temperature is slightly higher in the southern ecliptic hemisphere compared to the northern ecliptic hemisphere. It was originally observed in the Wilkinson Microwave Anisotropy Probe (WMAP) data (Eriksen et al. 2004, 2007; Hansen et al. 2009; Hoftuft et al. 2009; Paci et al. 2013; Prunet et al. 2005). The phenomenon has persisted in the Planck CMB temperature fluctuation data (Ade et al. 2014; Akrami et al. 2014; Ade et al. 2016; Rath & Jain 2013; Ghosh et al. 2016b).

The HPA is not the only observation of statistical isotropy (SI) violation. Other observations of SI violations include the CMB temperature quadrupole-octopole alignment (de Oliveira-Costa et al. 2004; Ralston & Jain 2004; Samal et al. 2008), the octopole planarity (Bennett et al. 2011), the CMB parity anomaly (Kim & Naselsky 2010;

Aluri & Jain 2012), the CMB temperature and polarization multipole alignments (Rath et al. 2018; Pinkwart & Schwarz 2018), the CMB Cold Spot (Cruz et al. 2005), the kinematic dipole excess in the large-scale structures (Singal 2011; Gibelyou & Huterer 2012; Rubart & Schwarz 2013; Tiwari et al. 2015; Tiwari & Jain 2015; Tiwari & Nusser 2016; Bengaly et al. 2018; Rameez et al. 2018), and the radio and optical polarization alignments (Hutsemekers 1998; Jain & Sarala 2006; Tiwari & Jain 2013) and radio dipole (Jain & Ralston 1999). A review of the SI violating phenomena can be found in Ghosh et al. (2016a).

Gordon (2007) proposed a dipole modulation model to explain HPA in temperature. According to this model, the observed temperature fluctuation field $\Delta T(\hat{n})$ can be written as:

$$\Delta T(\hat{n}) = \Delta \tilde{T}(\hat{n}) [1 + A \hat{\lambda} \cdot \hat{n}]. \quad (1)$$

Here $\Delta \tilde{T}(\hat{n})$ is a statistically isotropic field which is modulated by a cosine modulation term $\hat{\lambda} \cdot \hat{n}$ with an amplitude of A and direction $\hat{\lambda}$. There are other theoretical models which have been proposed in an attempt to explain the HPA in CMB temperature fluctuations (Groeneboom et al. 2010; Rath et al. 2013, 2015; Bridges et al. 2007; Boehmer & Mota 2008; Carroll et al. 2010; Erickcek et al. 2008, 2009; Emami et al. 2011; Aluri et al. 2011; Chang & Wang 2013; Cai et al. 2014; Zibin & Contreras 2017). A dipole modulation model, Eq. (1), as well as other theoretical models predict that one should be able to observe dipole modulation

* E-mail: shamik@iitk.ac.in

† E-mail: pkjain@iitk.ac.in

phenomenon in CMB polarization too (Namjoo et al. 2015; Kothari et al. 2016; Mukherjee & Souradeep 2015; Ghosh et al. 2016b; Contreras et al. 2017).

The estimators employed to search for the dipole modulation in the CMB temperature can be broadly classified as those methods working in multipole space with spherical harmonic coefficients of the CMB map (Hansen et al. 2009; Rath & Jain 2013; Zibin & Contreras 2017; Hajian & Souradeep 2003) and those methods which are applied on the maps directly in pixel space (Eriksen et al. 2004; Rath & Jain 2013; Akrami et al. 2014). For detection of dipole modulation in CMB polarization there are correspondingly different methods that work in multipole space (Basak et al. 2006; Ghosh et al. 2016b; Contreras et al. 2017) or pixel space (Aluri & Shafieloo 2017). There are also maximum likelihood-based estimation techniques employed for detecting HPA in CMB temperature and polarization (Gordon 2007; Hoftuft et al. 2009). In this work, we will introduce a procedure for estimating the dipole modulation amplitude and direction in pixel space using CMB polarized intensity maps.

2 THEORY

The signal of the CMB polarization is measured as Stokes parameters $Q(\hat{\mathbf{n}})$ and $U(\hat{\mathbf{n}})$. The quantity $P(\hat{\mathbf{n}}) = Q(\hat{\mathbf{n}}) + iU(\hat{\mathbf{n}})$ behaves as a spin-2 object while its complex conjugate $P^*(\hat{\mathbf{n}}) = Q(\hat{\mathbf{n}}) - iU(\hat{\mathbf{n}})$ behaves as a spin-(-2) object. When measured in an experiment the signal is observed along with instrumental noise. We write the resulting signal as:

$$\begin{aligned} P(\hat{\mathbf{n}}) &= P_s(\hat{\mathbf{n}}) + N_P(\hat{\mathbf{n}}) \\ P^*(\hat{\mathbf{n}}) &= P_s^*(\hat{\mathbf{n}}) + N_P^*(\hat{\mathbf{n}}). \end{aligned} \quad (2)$$

Here $P_s(\hat{\mathbf{n}}) = Q_s(\hat{\mathbf{n}}) + iU_s(\hat{\mathbf{n}})$ is the CMB polarization signal and $N_P(\hat{\mathbf{n}}) = N_Q(\hat{\mathbf{n}}) + iN_U(\hat{\mathbf{n}})$ is the combination instrumental noise in Q and U measurements. These quantities can be expanded in spin(± 2) spherical harmonics as:

$$P_X(\hat{\mathbf{n}}) = \sum_{\ell, m} a_{2, \ell m}^X 2Y_{\ell m}(\hat{\mathbf{n}}) = - \sum_{\ell, m} (a_{E, \ell m}^X + ia_{B, \ell m}^X) 2Y_{\ell m}(\hat{\mathbf{n}}) \quad (3)$$

$$\begin{aligned} P_X^*(\hat{\mathbf{n}}) &= \sum_{\ell, m} a_{-2, \ell m}^X 2Y_{\ell m}(\hat{\mathbf{n}}) \\ &= - \sum_{\ell, m} (a_{E, \ell m}^X - ia_{B, \ell m}^X) 2Y_{\ell m}(\hat{\mathbf{n}}) \\ &= - \sum_{\ell, m} (a_{E, \ell m}^{X*} - ia_{B, \ell m}^{X*}) 2Y_{\ell m}^*(\hat{\mathbf{n}}), \end{aligned} \quad (4)$$

with X being index for observed, signal or noise components of Eq. (2). Here $a_{E, \ell m}^X$ and $a_{B, \ell m}^X$ are the spherical harmonic coefficients of E-mode and B-mode polarization.

We will consider the dipole modulation in CMB polarization modelled as in Ghosh et al. (2016b). This modulation has been motivated from a physical perspective in Contreras et al. (2017). The CMB polarization signal $P_s(\hat{\mathbf{n}})$ is modulated as:

$$P_s(\hat{\mathbf{n}}) = \tilde{P}_s(\hat{\mathbf{n}}) \left(1 + A\hat{\lambda} \cdot \hat{\mathbf{n}}\right). \quad (5)$$

Here $\tilde{P}_s(\hat{\mathbf{n}})$ is the unmodulated isotropic polarization field, A and $\hat{\lambda}$ are the amplitude and direction of the dipole modulation respectively. The relation Eq. (5) would imply that the

modulation amplitude A is in general a complex number, as assumed by Ghosh et al. (2016b). However, modulation of the form in Eq. (5) results from a modulation of the temperature anisotropy quadrupole (Contreras et al. 2017). This implies that the modulation amplitude A is real. We point out that it is not possible to introduce the dipole modulation directly into the E mode polarization field (Kothari 2018). Furthermore the off-diagonal TE correlations are in general different from the corresponding ET correlations in the presence of dipole modulation (Kothari et al. 2016). From current observational evidence from CMB temperature anisotropies we can assume that the modulation amplitude is small and confine ourselves to first order in A . All the expressions written till now are for full sky observations. In reality, we only observe a fraction of the sky as galactic plane and point sources have to be masked during analysis. Let us assume a function $W(\hat{\mathbf{n}})$ as the mask function. We represent the observed masked sky CMB polarization as $P_{\text{obs}}(\hat{\mathbf{n}}) = P(\hat{\mathbf{n}})W(\hat{\mathbf{n}})$. This is given by:

$$P_{\text{obs}} = \tilde{P}_s(\hat{\mathbf{n}})W(\hat{\mathbf{n}}) \left(1 + A\hat{\lambda} \cdot \hat{\mathbf{n}}\right) + N_P(\hat{\mathbf{n}})W(\hat{\mathbf{n}}). \quad (6)$$

We are interested in the quantity $|P_{\text{obs}}(\hat{\mathbf{n}})|^2$ for a masked sky. We obtain

$$\begin{aligned} |P_{\text{obs}}(\hat{\mathbf{n}})|^2 &= |\tilde{P}_s(\hat{\mathbf{n}})|^2 W^2(\hat{\mathbf{n}}) \left(1 + 2A\hat{\lambda} \cdot \hat{\mathbf{n}}\right) \\ &\quad + \tilde{P}_s(\hat{\mathbf{n}})N_P^*(\hat{\mathbf{n}})W^2(\hat{\mathbf{n}}) \left(1 + A\hat{\lambda} \cdot \hat{\mathbf{n}}\right) \\ &\quad + \tilde{P}_s^*(\hat{\mathbf{n}})N_P(\hat{\mathbf{n}})W^2(\hat{\mathbf{n}}) \left(1 + 2A\hat{\lambda} \cdot \hat{\mathbf{n}}\right) \\ &\quad + |N_P(\hat{\mathbf{n}})|^2 W^2(\hat{\mathbf{n}}) \end{aligned} \quad (7)$$

We now substitute the expansion of these quantities from Eq. (3) and Eq. (4) and take realization average. For the unmodulated polarization field the realization average of the spherical harmonic coefficients satisfies:

$$\begin{aligned} \langle \tilde{a}_{E, \ell m} \tilde{a}_{E, \ell' m'}^* \rangle &= C_\ell^{EE} \delta_{\ell \ell'} \delta_{mm'} \\ \langle \tilde{a}_{B, \ell m} \tilde{a}_{B, \ell' m'}^* \rangle &= C_\ell^{BB} \delta_{\ell \ell'} \delta_{mm'} \\ \langle \tilde{a}_{E, \ell m} \tilde{a}_{B, \ell' m'}^* \rangle &= \langle \tilde{a}_{B, \ell m} \tilde{a}_{E, \ell' m'}^* \rangle = 0, \end{aligned} \quad (8)$$

In these expressions C_ℓ^{EE} and C_ℓ^{BB} are the CMB E-mode and B-mode power spectrum. While the noise satisfies:

$$\begin{aligned} \langle n_{E, \ell m} n_{E, \ell' m'}^* \rangle &= N_\ell^{EE} \delta_{\ell \ell'} \delta_{mm'} \\ \langle n_{B, \ell m} n_{B, \ell' m'}^* \rangle &= N_\ell^{BB} \delta_{\ell \ell'} \delta_{mm'} \\ \langle n_{E, \ell m} n_{B, \ell' m'}^* \rangle &= \langle n_{B, \ell m} n_{E, \ell' m'}^* \rangle = 0 \end{aligned} \quad (9)$$

along with $\langle \tilde{a}_{X, \ell m} n_{Y, \ell' m'}^* \rangle = \langle n_{X, \ell m} \tilde{a}_{Y, \ell' m'}^* \rangle = 0$, for X, Y in $\{E, B\}$. The quantities N_ℓ^{EE} and N_ℓ^{BB} are E-mode and B-mode noise power spectrum. Using relations Eq. (8) and Eq. (9) we can write the realization average of $|P_{\text{obs}}(\hat{\mathbf{n}})|^2$ as:

$$\begin{aligned} \langle |P_{\text{obs}}(\hat{\mathbf{n}})|^2 \rangle &= \sum_{\ell} \left[C_\ell^{EE} + C_\ell^{BB} \right] W^2(\hat{\mathbf{n}}) \left[1 + 2A\hat{\lambda} \cdot \hat{\mathbf{n}} \right] \\ &\quad \times \sum_m 2Y_{\ell m}(\hat{\mathbf{n}}) 2Y_{\ell m}^*(\hat{\mathbf{n}}) + \sum_{\ell} \left[N_\ell^{EE} + N_\ell^{BB} \right] \\ &\quad \times W^2(\hat{\mathbf{n}}) \sum_m 2Y_{\ell m}(\hat{\mathbf{n}}) 2Y_{\ell m}^*(\hat{\mathbf{n}}). \end{aligned} \quad (10)$$

Using the generalized addition theorem for Wigner D-

functions (Varshalovich et al. 1988), we obtain,

$$\sum_m 2Y_{\ell m}(\hat{\mathbf{n}})2Y_{\ell m}^*(\hat{\mathbf{n}}) = \frac{(2\ell+1)}{4\pi}, \quad (11)$$

Substituting back in our original expression Eq. (10) we get:

$$\begin{aligned} \langle |P_{\text{obs}}(\hat{\mathbf{n}}_i)|^2 \rangle = & W^2(\hat{\mathbf{n}}_i) \sum_{\ell} \left(\frac{2\ell+1}{4\pi} \right) \left\{ \left[\bar{C}_{\ell}^{EE} + \bar{C}_{\ell}^{BB} \right] \right. \\ & \left. \times \left[1 + 2A\hat{\lambda} \cdot \hat{\mathbf{n}}_i \right] + \left[\bar{N}_{\ell}^{EE} + \bar{N}_{\ell}^{BB} \right] \right\}. \quad (12) \end{aligned}$$

For realistic analysis we have replaced $\hat{\mathbf{n}}$ with $\hat{\mathbf{n}}_i$ of the i^{th} pixel and the barred power spectra represent adjustment for appropriate beam function and pixel window viz $\bar{C}_{\ell}^{XX} = C_{\ell}^{XX} B_{\ell}^2 F_{\ell}^2$. Note that B_{ℓ} is the beam function and F_{ℓ} is the pixel window function at the resolution at which we will perform the analysis.

2.1 Estimator construction

It is evident from Eq. (12) that $\langle |P|^2 \rangle$ will vary as a dipole due to the $\hat{\lambda} \cdot \hat{\mathbf{n}}$ term. We are interested in fitting this dipole for our parameters $\hat{\lambda}$ and A . For this fitting, we choose an i^{th} pixel to be the $\hat{\mathbf{z}}$ direction and divide the spherical sky into two hemispheres with the $\hat{\mathbf{z}}$ pointing outward through the center of the upper hemisphere and the $-\hat{\mathbf{z}}$ pointing outward through the center of the lower hemisphere. On each of the hemisphere, we can find the average value of our $|P|^2$ field. Then, for every choice of $\hat{\mathbf{z}}$ along i^{th} pixel, we can define two statistics R_i and D_i as follows:

$$R_i = \frac{\langle |P_{\text{obs}}(\hat{\mathbf{n}})|^2 \rangle_{U_i}}{\langle |P_{\text{obs}}(\hat{\mathbf{n}})|^2 \rangle_{D_i}} \quad (13)$$

$$D_i = \frac{\langle |P_{\text{obs}}(\hat{\mathbf{n}})|^2 \rangle_{U_i} - \langle |P_{\text{obs}}(\hat{\mathbf{n}})|^2 \rangle_{D_i}}{\langle |P_{\text{obs}}(\hat{\mathbf{n}})|^2 \rangle_{U_i} + \langle |P_{\text{obs}}(\hat{\mathbf{n}})|^2 \rangle_{D_i}}. \quad (14)$$

Here $\langle |P_{\text{obs}}(\hat{\mathbf{n}})|^2 \rangle_{U_i}$ and $\langle |P_{\text{obs}}(\hat{\mathbf{n}})|^2 \rangle_{D_i}$ denote the average value of the $|P_{\text{obs}}|^2$ field on the upper and lower hemispheres respectively for $\hat{\mathbf{z}}$ along $\hat{\mathbf{n}}_i$. We maximize these statistics by making a search over $\hat{\mathbf{z}}$. This resulting direction is the preferred axis $\hat{\lambda}$. Assuming that the dipole modulation effect is small both statistics will lead to the same result. Besides these we may also directly extract the dipole power as well as the dipole harmonic coefficients from the masked sky. The dipole power provides us with another estimate of the dipole modulation effect in data.

We next relate the maximal value of the statistics to the dipole modulation parameter A . For this we use the statistics D_i and note that the denominator is approximately the mean value of $|P|^2$ over the entire sky. Hence it remains fixed and D_i is maximized by simply maximizing the numerator. We first ignore the sky masking and assume full sky data. Using Eq. (12) and setting $\hat{\mathbf{z}} = \hat{\lambda}$ we obtain:

$$\begin{aligned} \left[\langle |P_{\text{obs}}(\hat{\mathbf{n}})|^2 \rangle_U - \langle |P_{\text{obs}}(\hat{\mathbf{n}})|^2 \rangle_D \right]_{\text{max}} = & \sum_{\ell} \left(\frac{2\ell+1}{4\pi} \right) \\ & \left(\bar{C}_{\ell}^{EE} + \bar{C}_{\ell}^{BB} \right) 2A. \quad (15) \end{aligned}$$

Hence we can write the estimator for the amplitude of modulation as:

$$\hat{A} = \frac{\left[\langle |P_{\text{obs}}(\hat{\mathbf{n}})|^2 \rangle_U - \langle |P_{\text{obs}}(\hat{\mathbf{n}})|^2 \rangle_D \right]_{\text{max}}}{\sum_{\ell} \left(\frac{2\ell+1}{2\pi} \right) \left(\bar{C}_{\ell}^{EE} + \bar{C}_{\ell}^{BB} \right)} \quad (16)$$

ν GHz	θ_{FWHM} [arcmin]	ΔT [μK arcmin]	ΔP [μK arcmin]
45	23.3	5.25	9.07
75	14.0	2.73	4.72
105	10.0	2.68	4.63
135	7.8	2.63	4.55
165	6.4	2.67	4.61
195	5.4	2.63	4.54
225	4.7	2.64	4.57
255	4.1	6.08	10.5
285	3.7	10.1	17.4
315	3.3	26.9	46.6
375	2.8	68.6	119
435	2.4	149	258
555	1.9	227	626
675	1.6	1320	3640
795	1.3	8070	22200

Table 1. CORE 4 year mission performance summary taken from The CORE Collaboration et al. (2011). Here ΔT and ΔP is the white noise level in μK in an arcmin size pixel in temperature and polarization respectively.

In the presence of masking with $W(\hat{\mathbf{n}}_i)$ the \hat{A} estimator changes as:

$$\hat{A} = \frac{\left[\langle |P_{\text{obs}}(\hat{\mathbf{n}})|^2 \rangle_U - \langle |P_{\text{obs}}(\hat{\mathbf{n}})|^2 \rangle_D \right]_{\text{max}}}{K \sum_{\ell} \left(\frac{2\ell+1}{2\pi} \right) \left(\bar{C}_{\ell}^{EE} + \bar{C}_{\ell}^{BB} \right)}, \quad (17)$$

where K is given by:

$$\begin{aligned} K = & \left\{ \int_U W^2(\hat{\mathbf{n}}) d\Omega \right\}^{-1} \int_U W^2(\hat{\mathbf{n}}) \cos \theta d\Omega \\ & - \left\{ \int_D W^2(\hat{\mathbf{n}}) d\Omega \right\}^{-1} \int_D W^2(\hat{\mathbf{n}}) \cos \theta d\Omega. \quad (18) \end{aligned}$$

We maximize the R and D statistics to find the preferred direction $\hat{\lambda}$. Along the direction $\hat{\lambda}$ we use the \hat{A} estimator to find the amplitude. We have tested this with isotropic and modulated simulations and used these with Planck 2015 polarization data.

3 SIMULATION

We used 2015 Planck cosmological parameters to generate the lensed power spectrum for scalar perturbations. This power spectrum is used with `synfast` facility from HEALPix¹ to create isotropic CMB sky maps. The simulation corresponding to Planck data is produced by using the effective temperature and polarization beams corresponding to the Commander or SMICA maps as provided by Planck. For our forecasts, we used Gaussian beams with FWHM equal to three times the pixel size.

3.1 Modulated Map Simulation

For our forecasts we modulated the masks along the hemispherical power asymmetry direction in temperature fluctuations, ($l = 232^\circ$, $b = -14^\circ$). We assume a modulation amplitude of $A = 0.07$ as observed in the CMB temperature data.

¹ <http://healpix.sourceforge.net>

For simplicity we assume $\hat{\lambda}$ along \hat{z} . Then $\hat{\lambda} \cdot \hat{n} = \sqrt{4\pi/3} Y_{10}(\hat{n})$. We can expand both sides of Eq. (5) in terms of the relations in Eq. (3) and Eq. (4) and write

$$a_{\pm 2, \ell m} = \tilde{a}_{\pm 2, \ell m} + A \sqrt{\frac{4\pi}{3}} \sum_{\ell' m'} \tilde{a}_{\pm 2, \ell' m'} \times \int_{\pm 2} Y_{\ell' m'}(\hat{n}) Y_{10}(\hat{n})_{\pm 2} Y_{\ell m}^*(\hat{n}) d\Omega. \quad (19)$$

We can write the integral of Eq. (19) in terms of Wigner-3j symbols using Gaunt's formula. Then rewriting $a_{\pm 2, \ell m}$ s in terms of $a_{E, \ell m}$ and $a_{B, \ell m}$ and using relations Eq. (3) and Eq. (4) we get:

$$a_{E, \ell m} = \tilde{a}_{E, \ell m} + A\alpha_- \tilde{a}_{E, \ell-1m} + iA\alpha_0 \tilde{a}_{B, \ell m} + A\alpha_+ \tilde{a}_{E, \ell+1m} \quad (20)$$

$$a_{B, \ell m} = \tilde{a}_{B, \ell m} + A\alpha_- \tilde{a}_{B, \ell-1m} - iA\alpha_0 \tilde{a}_{E, \ell m} + A\alpha_+ \tilde{a}_{B, \ell+1m}, \quad (21)$$

where,

$$\alpha_- = \frac{1}{\ell} \sqrt{\frac{(\ell-2)(\ell+2)(\ell-m)(\ell+m)}{(2\ell-1)(2\ell+1)}} \quad (22)$$

$$\alpha_0 = \frac{2m}{\ell(\ell+1)} \quad (23)$$

$$\alpha_+ = \frac{1}{\ell+1} \sqrt{\frac{(\ell-1)(\ell+3)(\ell-m+1)(\ell+m+1)}{(2\ell+1)(2\ell+3)}}. \quad (24)$$

These relations are identical to those in Contreras et al. (2017). During implementation, the isotropic maps are generated by `synfast` at resolution of `NSIDE=1024`. These maps are used to generate the isotropic $\tilde{a}_{X, \ell m}$ s. These are appropriately corrected for the beam function used in map generation and the pixel window function. We rotate the $\tilde{a}_{X, \ell m}$ of the isotropic map to align $\hat{\lambda}$ along \hat{z} . These $\tilde{a}_{X, \ell m}$ s are then modulated following (20) and (21). We perform appropriate rotations on the modulated $a_{X, \ell m}$ s to return the \hat{z} to the original direction. The modulated $a_{X, \ell m}$ s are readjusted with suitable pixel window function and beam function. The modulated map is synthesized from $a_{X, \ell m}$ s using `alm2map` utility.

3.2 Noise Simulation

For simulations for the Planck data maps, we use the half-ring half-difference (HRHD) maps and half-mission half-difference (HMHD) maps of the Commander and SMICA component separation methods as the noise proxy. Since the Planck noise and residual systematics are correlated between different multipoles, we do not attempt to simulate the Planck noise maps.

When simulating noise for a CORe-like mission, we use the sensitivity and design specifications from CORe white paper. We reproduce this data in table 1. With this data we generate the noise power spectrum using the following relation for instrumental noise as given by Errard et al. (2016):

$$N_{\ell}^{XX} = \left[\sum_{\nu} w_{X, \nu} \exp \left(-\ell(\ell+1) \frac{\theta_{\text{FWHM}, \nu}^2}{8 \ln 2} \right) \right]^{-1}. \quad (25)$$

Here $w_{T, \nu} = (\Delta T)^{-2}$ and $w_{E/B, \nu} = (\Delta P)^{-2}$. We used the values

of ΔT or ΔP , the sensitivity and θ_{FWHM} , the full width at half maximum in arc-minutes from table 1. Following Errard et al. (2016) we assume that there will be noise degradation due to component separation resulting in rescaling of N_{ℓ}^{XX} by a factor Δ which we assumed to be 1.5 for the present work. Hence the instrumental noise levels used in simulation was $\Delta \times N_{\ell}^{XX}$. We used `synfast` facility to generate random noise simulations from the noise power spectra. The noise maps are added to the simulated isotropic/modulated maps.

4 DATA

We use the 2015 Planck polarization data (release 2.02) for this work. We have worked with CMB maps produced by Commander and SMICA component separation procedures. It is well known that there are unexplained noise and residual systematics present in the polarization data (Adam et al. 2016b). The 2.02 data release does not have any large angular scale $\ell \leq 20$ polarization data as on these scales the data contains non-negligible systematics. The data is high pass filtered using the following cosine filtering with the polarization E-mode and B-mode (Adam et al. 2016c).

$$w_{\ell} = \begin{cases} 0 & \ell < 20 \\ \frac{1}{2} \left[1 - \cos \left(\pi \frac{\ell-20}{20} \right) \right] & 20 \leq \ell \leq 40 \\ 1 & 40 < \ell \end{cases} \quad (26)$$

Since scales corresponding to $\ell \geq 40$ are reliable we will limit ourselves to multipoles above this scale.

The Planck polarization maps are provided at HEALPix `NSIDE=1024`. We downgrade our maps to `NSIDE=64` for most of the analysis in this work. We use the following relation for downgrading our maps:

$$a_{\ell m}^{\text{OUT}} = \frac{a_{\ell m}^{\text{IN}} B_{\ell}^{\text{OUT}} F_{\ell}^{\text{OUT}}}{B_{\ell}^{\text{IN}} F_{\ell}^{\text{IN}}}. \quad (27)$$

Here B_{ℓ}^{IN} correspond to the instrumental beam at native resolution as provided by Planck and B_{ℓ}^{OUT} correspond to Gaussian beam for the output resolution. The functions F_{ℓ} correspond to the pixel window functions at input and output resolutions. Using Eq. (27) we prepare $a_{\ell m}$ s between $40 \leq \ell \leq 3\text{NSIDE}$. We use HEALPix subroutine `alm2map` to generate downgraded Q and U maps from these $a_{\ell m}$ s. We prepare $|P|^2$ maps by calculating $Q^2 + U^2$ in every pixel. For this work we used Planck Union polarization masks UPB77. The mask is not apodized.

5 METHOD

In section 2.1 we defined our direction and amplitude estimators for dipole modulation. We perform most our analysis with `NSIDE=64` maps. For this purpose Q and U maps are degraded using Eq. (27) and we produce P^2 maps by calculating $Q^2 + U^2$ pixel by pixel. For all our analysis on data or on simulated maps we have used the UPB77 mask. As described in section 2.1, we calculate R_i and D_i for every choice of \hat{z} on a `NSIDE=64` pixelized sphere. In our analysis, we remove the lower 40 multipoles when preparing the maps. We find the direction along which R or D maximizes. This gives us the direction $\hat{\lambda}$ of modulation. Along the direction

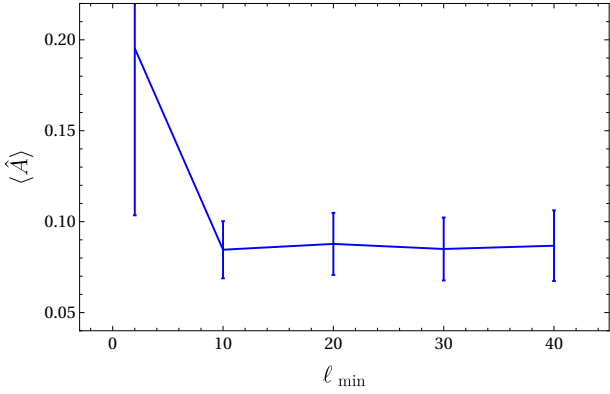


Figure 1. The plot shows the variation of the mean of the estimator \hat{A} with ℓ_{\min} using 150 simulated maps with input dipole modulation parameter $A = 0.07$. Here ℓ_{\min} is the multipole below which all modes are filtered out.

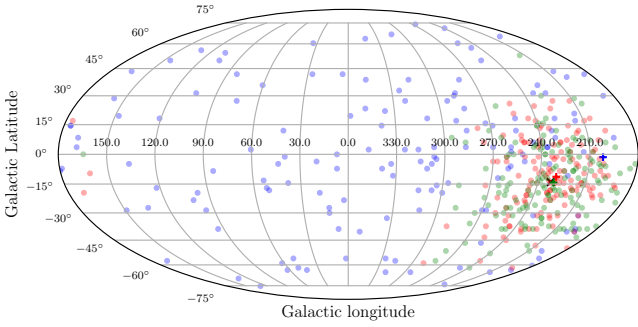


Figure 2. The scatter plot of the extracted directions using the R estimator. The blue markers are for $\ell_{\min} = 2$, red markers are for $\ell_{\min} = 10$ and green for $\ell_{\min} = 40$. The actual input direction is $l = 232^\circ, b = -14^\circ$, denoted by black 'x' and the '+' denotes the mean of the estimated values.

of maximum R and maximum D , we calculate the amplitude with use of Eq. (17). Note that the C_ℓ^{EE} and C_ℓ^{BB} used in Eq. (16) or Eq. (17) are multiplied with appropriate beam and pixel window functions.

5.1 Low- ℓ cut

The large angular scales, corresponding to the low- ℓ modes, have large uncertainties due to cosmic variance. Due to their large power contribution to the total sky power in large sky patches, such as a hemisphere, they significantly bias the mean value of the P^2 field. Since the low- ℓ modes show large fluctuation, their inclusion leads to a large bias in our estimators. In order to study this effect we generate 150 simulated maps with 7% modulation. The extracted dipole amplitude from these simulations is shown in figure 1 as a function of ℓ_{\min} . Here ℓ_{\min} represents the cutoff value such that for $\ell < \ell_{\min}$ we set all $a_{E,\ell m}$ and $a_{B,\ell m}$ to zero. After this filtering of the low- ℓ modes, we resynthesize Q and U maps for use in our analysis. We find that with no filtering the output of \hat{A} shows a large mean value with large uncertainties due to the fluctuations. In figure 2 we show the scatter plot of directions extracted from the R estimator for different values of ℓ_{\min} . We find that for no filtering $\ell_{\min} = 2$

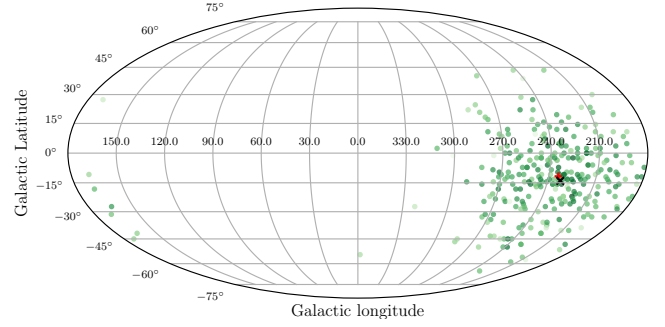


Figure 3. The extracted directions for 150 simulations with input $A = 0.07$ using the R estimator. The sky is masked with UPB77. The input value of $\hat{\lambda} = (l = 232^\circ, b = -14^\circ)$ is shown by the black 'x' and the mean of simulation is shown by red '+' symbols. Notice that the mean of estimated direction is nearly coincident with the input direction of the simulation. The plot for the D estimator is similar.

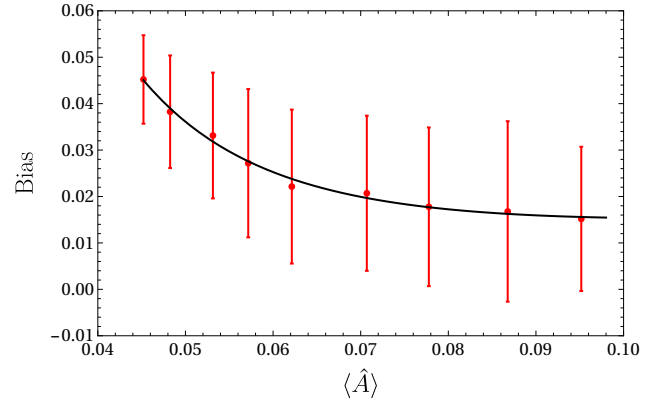


Figure 4. The variation of bias with \hat{A} mean is shown in this plot. The blue curve indicates the best-fit parametric model for bias.

(shown in blue) the directions show considerable scatter all over the sky. However the choice $\ell_{\min} = 10$ sufficiently removes the effects of cosmic variance. In figure 1 we see that with the variation of ℓ_{\min} from 10 to 40 in steps of 10, the mean of \hat{A} remains largely unchanged and furthermore, the variance for the estimator increases very slightly. In figure 2 the red markers plot the scatter for $\ell_{\min} = 10$ and green for $\ell_{\min} = 40$. The mean values of the direction estimator R is shown in red and green '+' markers for ℓ_{\min} of 10 and 40 respectively. These are very close to the actual direction used in the simulation. The uncertainty in the direction however increases with ℓ_{\min} .

For rest of the analysis in the paper, we will use $\ell_{\min} = 40$. The primary source of foreground contamination for CMB polarization measurements are polarized dust emissions. The E and B mode power spectra for the dust emissions have a power law behaviour $C_\ell^{XX} \propto \ell^{\alpha_{XX}}$ with a negative spectral index α_{XX} (Adam et al. 2016a). For $\ell < 40$ the polarized dust foreground is large, and there are additional systematic effects for 2015 Planck data which make $\ell < 40$ unreliable. In future experiments, we may recover the $\ell < 40$ modes better. For purposes of this work, including our forecast in the following subsection, we will make a con-

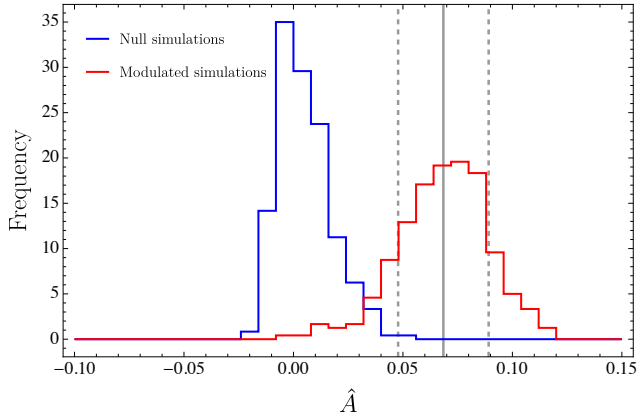


Figure 5. Distribution for the bias corrected amplitude for isotropic simulations (blue) and modulated (red) is plotted. The black line indicate the mean of the bias corrected amplitude for the modulated simulation data. The two dashed lines on either side represent 1σ width around the mean.

MAP	Amplitude	$\hat{\lambda}$	p-value
Commander	0.136	($l = 280^\circ b = 45^\circ$)	0.83
SMICA	0.123	($l = 247^\circ b = 45^\circ$)	0.99

Table 2. Planck 2015 polarization results for Commander and SMICA maps at $\text{NSIDE} = 64$. The bias uncorrected amplitude and the direction of modulation is provided. We also provide the p-value for the corresponding result using HRHD. The errors in the estimated amplitude and direction are discussed in the text.

NSIDE	Amplitude	$\hat{\lambda}$
64	0.136	($280.5^\circ, 45.0^\circ$)
128	0.100	($250.5^\circ, 45.0^\circ$)
256	0.080	($249.8^\circ, 46.6^\circ$)
512	0.054	($355.0^\circ, 76.8^\circ$)

Table 3. Results for bias uncorrected amplitude of dipole modulation and direction of modulation for different resolutions of the Commander polarization map.

servative assumption that $\ell < 40$ are unreliable. We should also note that if the dipole modulation is scale dependent, with reduced effect at smaller scales, $\ell < 40$ modes could be important for significant detection.

5.2 Estimator performance and bias correction

We use simulated CMB maps which are modulated as described in 3.1. Noise maps, prepared with CORE specifications, as discussed in 3.2, are added to the simulated maps. We prepared P^2 maps as discussed above and estimated the direction $\hat{\lambda}$ with R and D estimators as described above. The scatter plot for the R estimator is shown in figure 3. The corresponding plot for D estimator is similar. We note that both the R and D estimators maximize along exactly same directions. For masked sky the mean reconstructed direction is ($234^\circ \pm 28^\circ, -12^\circ \pm 19^\circ$) for both the R and D estimators. We can see that both the estimators have a nearly negligible

bias. The R and D estimators can be assumed to be unbiased estimators for the direction of modulation. There is $\sim 20^\circ$ error in the estimated direction coordinates.

The amplitude estimator defined in Eq. (17) is a biased estimator. The bias varies with the modulation amplitude. To study and characterize the bias in \hat{A} we performed simulations with different modulation amplitudes from 0.0 to 0.8 in steps of 0.01. For each input modulation amplitude, we performed 150 simulations using the process described in section 3 for CORE-like noise. We estimated the amplitude using the pipeline described above and from these estimates calculated the mean bias corresponding to the mean value of \hat{A} . The error in the bias is calculated from the standard deviation of \hat{A} . The plot of the bias values versus the \hat{A} mean is shown in figure 4. The bias is large for no modulation or small modulation amplitudes. It decreases and attains a steady value for larger modulation amplitudes. The bias decreases with a decrease in the skewness of the underlying distribution.

We use the simulated data to derive a parametric model for our \hat{A} estimator bias. Our assumed bias model $b(\hat{A})$ is:

$$b(\hat{A}) = \beta_0 + \beta_1 \hat{A}^{-1} + \beta_2 \hat{A}^{-2}. \quad (28)$$

We use our simulated data to fit the parameters β_0 , β_1 and β_2 . The best-fit parameter values are $\beta_0 = 0.03014 \pm 0.00698$, $\beta_1 = -0.00325 \pm 0.00088$ and $\beta_2 = 0.000177 \pm 0.000026$. We use this parametric bias model in our forecast for a CORE-like experiment. We calculate the bias-corrected amplitude as $\hat{A}_c = \hat{A} - b(\hat{A})$. During implementation on the null distribution, we note that this bias correction model should be applied only to the mean of the distribution to estimate the bias for all samples of the null simulation. This is because the bias correction model overcompensates for small values of \hat{A} . This results in the least biased values for the null distribution in having the largest bias correction. The skewness of the null distribution also affects the bias correction when applied to individual samples of the null distribution. However, at larger values of modulation amplitude, the bias correction model works reliably when applied to individual samples of the distribution. We would point out that the bias model is dependent on our noise model. It is also understandable that the bias model that is assumed here would work fairly well for $10 \leq \ell_{\min} \leq 40$, a multipole region which is eliminated from our analysis, since the result for \hat{A} is fairly agnostic of the ℓ_{\min} value as long as the largest scales have been removed.

5.3 Forecast for CORE-like experiment

In figure 5 we present our forecast for a CMB polarization modulation with an amplitude of 0.07 with CORE-like instrumental noise. We simulated these results with the cut $\ell \geq 40$. We applied the bias correction model to the mean of the null distribution and to individual samples of the modulated sky simulations. This method is realistic since we can estimate the mean of the null distribution from simulation but not necessarily the mean of the actual CMB sky. The direction observations with a masked sky would follow figure 3. From figures 3 and 5 it is apparent that a 7% dipole modulation of the kind observed in CMB temperature fluctuations should be detectable at over 3σ with a CORE-like full sky experiment. We should also be able to estimate the

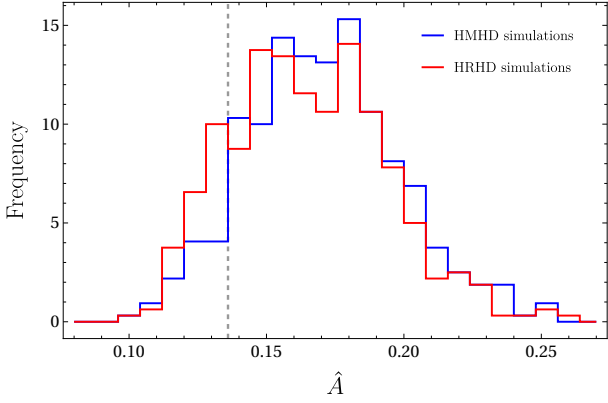


Figure 6. The null distribution for \hat{A} with HMHD and HRHD noise proxies are shown for Commander. The black dashed line represent the observed value for Commander from table 2

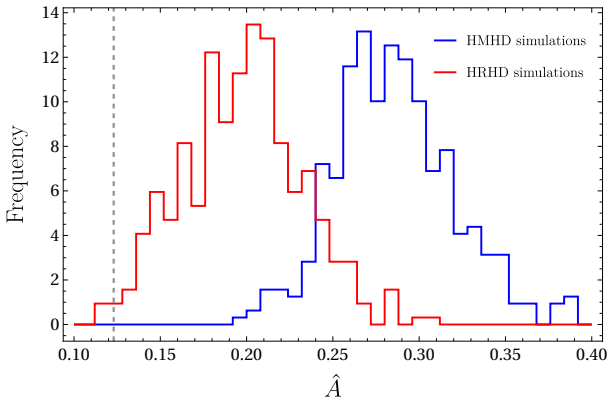


Figure 7. The null distribution for \hat{A} with HMHD and HRHD noise proxies are shown for SMICA in this figure. The black dashed lines represent the observed value for SMICA from table 2.

direction with acceptable errors. The above discussion provides justification for the use of our pixel space estimators for detecting dipole modulation in CMB polarization in future experiments.

6 RESULTS

We have analyzed 2015 Planck CMB polarization maps cleaned by Commander and SMICA component separation methods. The results for bias uncorrected amplitude is provided in table 2. We use the standard deviation of the HRHD null simulations to determine the relative error we can expect with our \hat{A} estimator. The histograms for our null distributions are shown in figures 6 and 7. The grey dashed line indicates the observed amplitude from the corresponding Planck map. The error in the Commander result is ± 0.023 while the error in the SMICA result is ± 0.021 . These are statistical errors and given the extracted amplitude in table 2 suggest the presence of a strong signal in data. However, as we shall see below there also exists a strong bias or systematic effect which appears to mask any real effect which may be present in data. We do not perform any bias correction for these results due to the unavailability of polarization noise

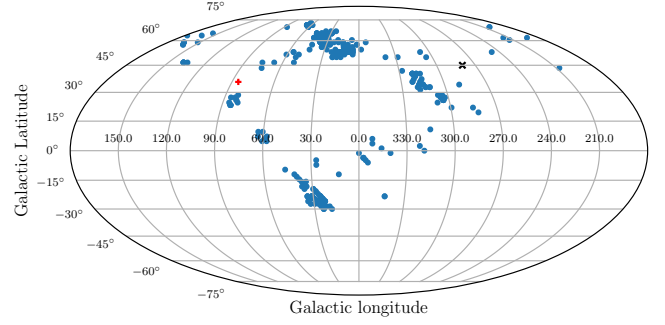


Figure 8. The scatter of direction of modulation from R statistic is plotted for Commander HMHD noise proxy. The direction observed in the respective data is denoted by the black cross marker. The mean direction from the simulations is shown by the red plus marker.

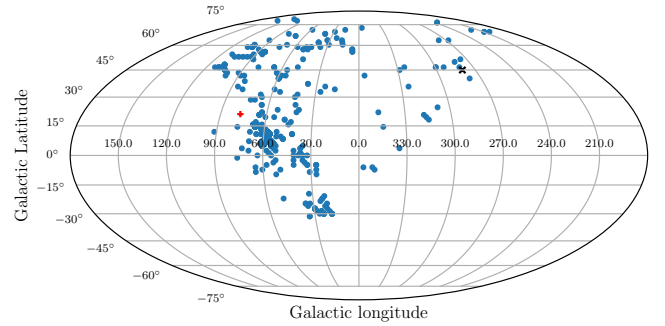


Figure 9. The scatter of direction of modulation from R statistic is plotted for Commander HRHD noise proxy. The direction observed in the respective data is denoted by the black cross marker. The mean direction from the simulations is shown by the red plus marker.

simulations which have been propagated through the component separation methods. We estimated the significance of our results using 400 isotropic simulations as described in section 3. We used either the corresponding HRHD or HMHD maps as noise proxies as discussed in section 3.2. The p-values quoted in table 2 are for HRHD noise proxies. With HMHD noise proxies, the p-values for Commander and SMICA maps are 0.90 and 1.0 respectively. This means that most of the randomly generated samples lead to statistics values larger than those seen in data. Since the spread in the HRHD (or HMHD) null distributions is relatively small the large p-values indicate the presence of large bias in the detector noise.

We also determine the dipole power from the masked sky and compare it with the corresponding result from simulations. This leads to a p-value of 0.71 with HRHD, which is also large but a little smaller than that obtained with other statistics. Hence the result obtained with dipole power is consistent with other statistics.

The scatter plots for the directions from the simulations are shown in figures 8 to 11. We indicate the observed direction in the data by the black cross. The red plus symbol in these plots denotes the mean value of the directions from the simulations. We note strong clustering in all sets of simulations. The clustering is larger for the simulation

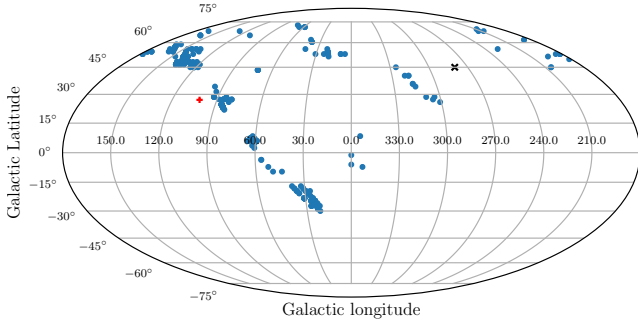


Figure 10. The scatter of direction of modulation from R statistic is plotted for SMICA HMHD noise proxy. The direction observed in the respective data is denoted by the black cross marker. The mean direction from the simulations is shown by the red plus marker.

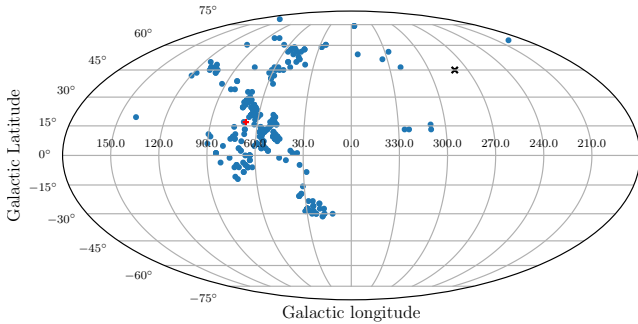


Figure 11. The scatter of direction of modulation from R statistic is plotted for SMICA HRHD noise proxy. The direction observed in the respective data is denoted by the black cross marker. The mean direction from the simulations is shown by the red plus marker.

with HMHD in figures 8 and 10 than for the simulations with HRHD proxies as in figures 9 and 11. However, the direction of the clustering is very different from the direction observed in the data.

In table 3 we show the effect of varying the resolution of the P^2 map on the analysis. We see that the effect of modulation decreases with increase in resolution. We also see that the direction of the effect migrates towards the galactic pole with an increase in resolution.

Our results for the Planck 2015 polarization data largely agree with previous results (Ghosh et al. 2016b; Aluri & Shafieloo 2017). The direction of modulation recovered from the Planck 2015 Commander polarization data agree closely with the results of Ghosh et al. (2016b) in 40-100 multipole range while the direction from their 40-125 multipole range is within the error bounds of the result. Our results for the direction are in good agreement with those obtained from local variance maps (Aluri & Shafieloo 2017). All the direction results are consistent with Aluri & Shafieloo (2017) with lower- ℓ cut of 60 or 100. While Ghosh et al. (2016b) does not give a result for dipole modulation amplitude, the modulation amplitude result from Aluri & Shafieloo (2017) is much smaller than the results we obtain. This is likely due to the difference in the way the two methods deal with correlated noise when estimating the model parameter values.

However, unlike Aluri & Shafieloo (2017) we do not find our results to be significant when comparing with simulations including HMHD and HRHD noise proxies. These indicate a large correlated noise/residual systematics which may not have been included in the simulations performed by Aluri & Shafieloo (2017).

The direction obtained in the CMB polarization data is very different from simulations having HRHD or HMHD noise proxies. If we take the noise proxies seriously, the clustering seen in noise simulations implies that there is a very large bias in data. We attempt to correct for this bias by subtracting the mean value of the dipole modulation effect seen in noise simulations. We use the results for HRHD for this purpose which show clustering predominantly about a single direction. We define a quantity d as

$$d = \frac{[\langle |P(\hat{n})|^2 \rangle_U - \langle |P(\hat{n})|^2 \rangle_D]_{\max}}{K}. \quad (29)$$

We estimate the quantity d from our isotropic simulation with HRHD noise proxies and call this d_N . The d estimated from data is d_T . The d_N and d_T are dipole modulation in simulations and data respectively. We subtract d_N from d_T vectorially to obtain the dipole modulation signal. For the Commander map with NSIDE=64, we obtain $d_N = (1.01 \pm 0.18) \times 10^{-14} \text{ K}^2$. The corresponding mean direction is found to be $(77^\circ, 22^\circ)$ in galactic coordinates, which is close to the ecliptic pole. The resulting bias corrected values of the parameters are found to be $A = 0.24$ with preferred direction $(266^\circ, 7.2^\circ)$. The corresponding parameters for SMICA are $A = 0.28$ with preferred direction $(246^\circ, 7.2^\circ)$. Both are consistent with one another and the amplitude is rather large. Hence this suggests the presence of an effect in data. However due to our poor understanding of noise or residual systematics present in data we are unable to claim reliable removal of the bias. More understanding of the noise and systematics is needed to make any significant detection of a cosmological dipole modulation signal.

7 CONCLUSIONS

We have developed a pixel based method to test for dipole modulation effect in CMB polarization. The method is based on directly using the observed polarized flux $|P|^2 = Q^2 + U^2$ and can be implemented easily on masked sky. We have proposed a simple statistics in order to characterize the effect. The statistic quantifies the difference in the mean value of $|P|^2$ in two hemispheres along some chosen direction. Alternatively one can directly extract the dipole harmonic coefficients from data. We have determined the performance of our statistics for a future CORe-like mission. We find that if the effect is present in data at the level expected from the dipole modulation seen in CMB temperature, it should be detectable at better than 3σ level. We also apply our method to Planck CMB polarization data. It is well known that this data contains some unknown bias and is not reliable for study of large scale isotropy. We find that the dipole modulation is present in data in a direction roughly coincident with the CMB temperature dipole. The amplitude is found to be relatively large, however the null simulations using HRHD and HMHD noise proxies show an even larger effect. We find that this effect shows clustering in a direction which is very different to that seen in real data. Hence

this represents a potential bias that may be present in data. We subtract this bias vectorially from the dipole modulation seen in real data. The resulting dipole modulation parameters provide our best estimate for the effect. However since the data is not reliable we are unable to make any definitive claims about violation of isotropy.

ACKNOWLEDGEMENTS

The authors acknowledge funding from the Science and Engineering Research Board (SERB), Government of India, for this research project. Some of the results in this paper have been derived using the HEALPix (GÅrski et al. 2005) package. We acknowledge the use of 2015 Planck polarization data, available through the Planck Legacy Archive, for some results in this paper.

REFERENCES

- Adam R., et al., 2016a, *Astron. Astrophys.*, 586, A133
- Adam R., et al., 2016b, *A&A*, 594, A1
- Adam R., et al., 2016c, *Astron. Astrophys.*, 594, A9
- Ade P. A. R., et al., 2014, *Astron. Astrophys.*, 571, A23
- Ade P. A. R., et al., 2016, *Astron. Astrophys.*, 594, A16
- Akrami Y., Fantaye Y., Shafieloo A., Eriksen H. K., Hansen F. K., Banday A. J., GÅrski K. M., 2014, *Astrophys. J.*, 784, L42
- Aluri P. K., Jain P., 2012, *Mon. Not. Roy. Astron. Soc.*, 419, 3378
- Aluri P. K., Shafieloo A., 2017, preprint, ([arXiv:1710.00580](https://arxiv.org/abs/1710.00580))
- Aluri P. K., Samal P. K., Jain P., Ralston J. P., 2011, *Mon. Not. Roy. Astron. Soc.*, 414, 1032
- Basak S., Hajian A., Souradeep T., 2006, *Phys. Rev.*, D74, 021301
- Bengaly C. A. P., Maartens R., Santos M. G., 2018, *JCAP*, 1804, 031
- Bennett C. L., et al., 2011, *Astrophys. J. Suppl.*, 192, 17
- Boehmer C. G., Mota D. F., 2008, *Phys. Lett.*, B663, 168
- Bridges M., McEwen J. D., Lasenby A. N., Hobson M. P., 2007, *Mon. Not. Roy. Astron. Soc.*, 377, 1473
- Cai Y.-F., Zhao W., Zhang Y., 2014, *Phys. Rev.*, D89, 023005
- Carroll S. M., Tseng C.-Y., Wise M. B., 2010, *Phys. Rev.*, D81, 083501
- Chang Z., Wang S., 2013, *Eur. Phys. J.*, C73, 2516
- Contreras D., Zibin J. P., Scott D., Banday A. J., GÅrski K. M., 2017, *Phys. Rev. D*, 96, 123522
- Cruz M., Martinez-Gonzalez E., Vielva P., Cayon L., 2005, *Mon. Not. Roy. Astron. Soc.*, 356, 29
- Emami R., Firouzjahi H., Sadegh Movahed S. M., Zarei M., 2011, *JCAP*, 1102, 005
- Erickcek A. L., Kamionkowski M., Carroll S. M., 2008, *Phys. Rev.*, D78, 123520
- Erickcek A. L., Hirata C. M., Kamionkowski M., 2009, *Phys. Rev.*, D80, 083507
- Eriksen H. K., Hansen F. K., Banday A. J., Gorski K. M., Lilje P. B., 2004, *Astrophys. J.*, 605, 14
- Eriksen H. K., Banday A. J., Gorski K. M., Hansen F. K., Lilje P. B., 2007, *Astrophys. J.*, 660, L81
- Errard J., Feeney S. M., Peiris H. V., Jaffe A. H., 2016, *JCAP*, 1603, 052
- Ghosh S., Jain P., Kashyap G., Kothari R., Nadkarni-Ghosh S., Tiwari P., 2016a, *J. Astrophys. Astron.*, 37, 25
- Ghosh S., Kothari R., Jain P., Rath P. K., 2016b, *Journal of Cosmology and Astroparticle Physics*, 2016, 046
- Gibelyou C., Huterer D., 2012, *Mon. Not. Roy. Astron. Soc.*, 427, 1994
- Gordon C., 2007, *Astrophys. J.*, 656, 636
- Groeneboom N. E., Axelsson M., Mota D. F., Koivisto T., 2010, preprint, ([arXiv:1011.5353](https://arxiv.org/abs/1011.5353))
- GÅrski K. M., Hivon E., Banday A. J., Wandelt B. D., Hansen F. K., Reinecke M., Bartelmann M., 2005, *The Astrophysical Journal*, 622, 759
- Hajian A., Souradeep T., 2003, *Astrophys. J.*, 597, L5
- Hansen F. K., Banday A. J., Gorski K. M., Eriksen H. K., Lilje P. B., 2009, *Astrophys. J.*, 704, 1448
- Hoftuft J., Eriksen H. K., Banday A. J., Gorski K. M., Hansen F. K., Lilje P. B., 2009, *Astrophys. J.*, 699, 985
- Hutsemekers D., 1998, *Astron. and Astrophys.*, 332, 410
- Jain P., Ralston J. P., 1999, *Mod. Phys. Lett.*, A14, 417
- Jain P., Sarala S., 2006, *J. Astrophys. Astron.*, 27, 443
- Kim J., Naselsky P., 2010, *Astrophys. J.*, 714, L265
- Kothari R., 2018, preprint, ([arXiv:1806.06325](https://arxiv.org/abs/1806.06325))
- Kothari R., Ghosh S., Rath P. K., Kashyap G., Jain P., 2016, *Mon. Not. Roy. Astron. Soc.*, 460, 1577
- Mukherjee S., Souradeep T., 2015, preprint, ([arXiv:1504.02285](https://arxiv.org/abs/1504.02285))
- Namjoo M. H., Abolhasani A. A., Assadollahi H., Baghran S., Firouzjahi H., Wands D., 2015, *JCAP*, 1505, 015
- Paci F., Gruppuso A., Finelli F., De Rosa A., Mandolesi N., Natoli P., 2013, *Mon. Not. Roy. Astron. Soc.*, 434, 3071
- Pinkwart M., Schwarz D. J., 2018, preprint, ([arXiv:1803.07473](https://arxiv.org/abs/1803.07473))
- Prunet S., Uzan J.-P., Bernardeau F., Brunier T., 2005, *Phys. Rev.*, D71, 083508
- Ralston J. P., Jain P., 2004, *Int. J. Mod. Phys.*, D13, 1857
- Rameez M., Mohayae R., Sarkar S., Colin J., 2018, *Mon. Not. Roy. Astron. Soc.*, 477, 1772
- Rath P. K., Jain P., 2013, *JCAP*, 1312, 014
- Rath P. K., Mudholkar T., Jain P., Aluri P. K., Panda S., 2013, *JCAP*, 1304, 007
- Rath P. K., Aluri P. K., Jain P., 2015, *Phys. Rev.*, D91, 023515
- Rath P. K., Samal P. K., Panda S., Mishra D. D., 2018, *Mon. Not. Roy. Astron. Soc.*, 475, 4357
- Rubart M., Schwarz D. J., 2013, *Astron. Astrophys.*, 555, A117
- Samal P. K., Saha R., Jain P., Ralston J. P., 2008, *Mon. Not. Roy. Astron. Soc.*, 385, 1718
- Singal A. K., 2011, *Astrophys. J.*, 742, L23
- The CORe Collaboration et al., 2011, preprint, ([arXiv:1102.2181](https://arxiv.org/abs/1102.2181))
- Tiwari P., Jain P., 2013, *International Journal of Modern Physics D*, 22, 1350089
- Tiwari P., Jain P., 2015, *Mon. Not. Roy. Astron. Soc.*, 447, 2658
- Tiwari P., Nusser A., 2016, *JCAP*, 1603, 062
- Tiwari P., Kothari R., Naskar A., Nadkarni-Ghosh S., Jain P., 2015, *Astropart. Phys.*, 61, 1
- Varshalovich D. A., Moskalev A. N., Khersonskii V. K., 1988, *Quantum Theory of Angular Momentum*. World Scientific Publishing Co, doi:10.1142/0270
- Zibin J. P., Contreras D., 2017, *Phys. Rev.*, D95, 063011
- de Oliveira-Costa A., Tegmark M., Zaldarriaga M., Hamilton A., 2004, *Phys. Rev.*, D69, 063516

This paper has been typeset from a $\text{\TeX}/\text{\LaTeX}$ file prepared by the author.